RSC Advances

PAPER

View Article Online
View Journal | View Issue

Cite this: *RSC Adv.*, 2023, **13**, 5674

In situ synthesis of a Bi_2O_3 quantum dot decorated BiOCl heterojunction with superior photocatalytic capability for organic dye and antibiotic removal

Mingliang Zhang,[ab] Fangfang Duo,[b] Jihong Lan,[b] Jianwei Zhou,[b] Liangliang Chu,[b] Chubei Wang[b] and Lixiang Li *[ac]

Received 4th December 2022
Accepted 24th January 2023

DOI: 10.1039/d2ra07726d

rsc.li/rsc-advances

As a decoration method, coupling a photocatalyst with semiconductor quantum dots has been proven to be an efficient strategy for enhanced photocatalytic performance. Herein, a novel BiOCl nanosheet decorated with Bi_2O_3 quantum dots (QDs) was first synthesized by a facile one-step *in situ* chemical deposition method at room temperature. The as-prepared materials were characterized by multiple means of analysis. The Bi_2O_3QDs with an average diameter of about 8.0 nm were uniformly embedded on the surface of BiOCl nanosheets. The obtained Bi_2O_3QDs/BiOCl exhibited significantly enhanced photocatalytic performance on the degradation of the rhodamine B and ciprofloxacin, which could be attributed to the band alignment, the photosensitization effect and the strong coupling between Bi_2O_3 and BiOCl. In addition, the dye photosensitization effect was demonstrated by the monochromatic photodegradation experiments. The radical trapping experiments and the ESR testing demonstrated the type II charge transfer route of the heterojunction. Finally, a reasonable photocatalytic mechanism based on the relative band positions was discussed to illustrate the photoreaction process. These findings provide a good choice for the design and potential application of BiOCl-based photocatalysts in water remediation.

1. Introduction

With the excessive consumption of fossil fuels, the energy sources shortage and environmental pollution have led to threats to social development and economic growth.[1–3] In this case, semiconductor photocatalysis, as an advanced oxidation technology, has been widely investigated in recent years for its potential application in degrading organic pollutants and water splitting.[4–6] To date, great attention has been paid to bismuth oxychloride (BiOCl) due to its unique 2D layered structure and strong oxidizing ability on organic contaminants. The layered structure consists of $[Bi_2O_2]^{2+}$ slabs interleaved by double chlorine atoms along the [001] direction of BiOCl,[7–9] which can facilitate the transfer and separation of photo-induced carriers. Nevertheless, the relatively wide band gap ($E_g = 3.2–3.6$ eV) and the poor quantum efficiency limit the application of BiOCl under the visible light region.[10,11] Among the modifications on the semiconductor photocatalysts, comparing with morphology control,[12,13] crystal facet regulation,[14] noble metal doping,[15] defect engineering[16] and element deposition,[17] to construct heterojunction with other semiconductor materials has been regarded as one of the most effective strategies to improve the photocatalytic performance, which can build an internal electric field between the contact surface of the two components to improve the separation efficiency of the photogenerated electron–hole pairs.[18–21]

As a low-cost, eco-friendliness, stability, low-toxicity and narrow band gap ($E_g = 2.6–2.8$ eV) photocatalyst, Bi_2O_3 has been considered as a promising candidate to construct heterojunction photocatalyst. Since Chai *et al.*[22] firstly reported the heterojunctioned BiOCl/Bi_2O_3 and its application in the degradation of aqueous 1,4-terephthalic acid. The BiOCl/Bi_2O_3 heterojunctions have been comprehensively studied with various methods and multifaceted application in the degrading organic dyes and antibiotics.[23,24] For example, Teng *et al.*[25] developed a green method for synthetizing α-Bi_2O_3/BiOCl composite material and investigated its excellent photocatalytic performance during the degradation of RhB. Kong *et al.*[26] and Ruiz-Castillo *et al.*[27] successfully prepared Bi_2O_3/BiOCl heterojunction by treating the Bi_2O_3 with different stoichiometric amounts of HCl and studied its outstanding photocatalytic activity for the degradation of the tetracycline hydrochloride and caffeine, respectively. Recently, the Bi_2O_3 quantum dots

---

[a] Key Laboratory of Energy Materials and Electrochemistry Liaoning Province, School of Chemical Engineering, University of Science and Technology Liaoning, 185 Qianshanzhong Road, Anshan 114051, Liaoning, China. E-mail: lxli2005@126.com; Tel: +86 13841291383

[b] Henan Photoelectrocatalytic Material and Micro-nano Application Technology Academician Workstation, Xinxiang University, Xinxiang 453003, Henan, China

[c] State Key Laboratory of Marine Resource Utilization in South China Sea, Hainan Provincial Key Lab of Fine Chemistry, School of Chemical Engineering and Technology, Hainan University, Haikou 570228, China

have received abundant attention due to unique particle size effect and multiple excitons, which can distinctly improve the photocatalytic efficiency.[28] Lv *et al.*[29] prepared a novel Bi_2O_3QDs/$BiVO_4$ heterojunctions which showed the enhanced photocatalytic activity than pure $BiVO_4$ nanofibers. Lou *et al.*[30] used three different photochemical methods to prepare TiO_2 decorated by the Bi_2O_3QDs, and revealed that Bi_2O_3QDs deposited on electron-rich sites of TiO_2 could provide a facile separation and transfer channel for the photogenic electron hole pairs. According to the above reports, the Bi_2O_3 quantum dots could be an ideal candidate to couple with 2D BiOCl to construct the 0D/2D semiconductor heterojunctions. As for as we know, to prepare Bi_2O_3QDs decorated BiOCl nanosheets with a facile *in situ* formation strategy have not been reported before this paper.

In this work, Bi_2O_3QDs/BiOCl heterojunction photocatalyst has been successfully prepared by a simple *in situ* chemical deposition method at room temperature. The X-ray powder diffraction (XRD), Fourier transform infrared spectroscopy (FT-IR), Raman spectrum, scanning electron microscopy (SEM), transmission electron microscopy (TEM), UV-vis diffusion reflectance spectroscopy (DRS), X-ray photoelectron spectroscopy (XPS), electron spin resonance (ESR), Brunauer–Emmett–Teller specic surface area (BET) and photoluminescence spectra (PL) were carried out to investigate the structure, morphology, elemental composition and optical absorption properties of the composites. The photocatalytic activity of as-prepared composites were investigated by photo-degrading of rhodamine B (RhB) and ciprofloxacin (CIP) under the visible light irradiation and the simulated sunlight, respectively. The results show that the heterojunction between Bi_2O_3QDs and BiOCl plays a crucial role on enhancing photocatalytic performance, which can promote the charge transfer in the reaction process.

2. Experimental section

2.1 Materials

Sodium bismuthate dihydrate ($NaBiO_3 \cdot 2H_2O$) was obtained from Hubei xinkang pharmaceutical chemical Co., Ltd (Tianmen, China). Rhodamine B (RhB) was purchased from Sinopharm Chemical Reagent Co., Ltd, China. Ciprofloxacin (CIP) was obtained from Beijing Solarbio Science and Technology Co., Ltd (Beijing, China). Absolute ethyl alcohol was supplied by Jinan Mingxin Chemical Co., Ltd (Jinan, China). Potassium iodide (KI) was obtained from Fuchen Chemical Reagent Co., Ltd, (Tianjin, China). Potassium chloride (KCl) was supplied by Deen Reagent Co., Ltd, (Tianjin, China). Hydrochloric acid (HCl) was provided by the Luoyang Haohua Chemical Reagent Co., Ltd, (Luoyang, China). Sodium hydroxide (NaOH) was purchased by Hebei Jiuxing Chemical Products Co., Ltd, (Hebei, China). *p*-Benzoquinone was purchased from Sinopharm Chemical Reagent Co., Ltd, China. Tertiary butanol alcohol ($(CH_3)_3COH$) was obtained from Jinan Mingwei Chemical Industry Co., Ltd, (Jinan, China). Disodium ethylenediaminetetraacetate (EDTA-2Na) was provided by Jinan Fengsheng Chemical Industry Co., Ltd, (Jinan, China). All the drugs and reagents were analytically purity without further purification, deionized water was used through all the experiments.

2.2 Preparation of Bi_2O_3QDs/BiOCl and BiOCl

Scheme 1 illustrates the synthesis of the Bi_2O_3QDs/BiOCl heterojunction. Typically, 3 mmol $NaBiO_3 \cdot 2H_2O$ was dissolved in 30 mL ethanol and 6 mmol KI was dissolved in 20 mL hydrochloric acid (2 mol L^{-1}), respectively. Then, the KI aqueous solution was dropped into the $NaBiO_3$ solution to form the mixture A. Subsequently, 3 mmol KCl dissolved into 10 mL NaOH solution (2 mol L^{-1}) was added into the mixture A and kept stirring for 2 h in the darkness. The resulting precipitate was collected by the centrifuged method and washed with ethanol and deionized water for three times. Finally, the white powers were obtained by drying in an air circulating oven at 60 °C.

For comparison, bismuth oxychloride was prepared by the similar procedure without sodium hydroxide. 3 mmol $NaBiO_3 \cdot 2H_2O$ was dissolved in 30 mL ethanol and 6 mmol KI was dissolved in 20 mL hydrochloric acid (2 mol L^{-1}), respectively. Then, the KI aqueous solution was dropped into the $NaBiO_3$ solution to form the mixture A. Subsequently, 0.3 mol L^{-1} KCl aqueous solution (10 mL) was added into the mixture A and kept stirring for 2 h in the darkness. The resulting precipitate was collected by the centrifuged method and washed with ethanol and deionized water for three times.

2.3 Materials characterization

The X-ray diffraction (XRD, Bruker D8 Advance) with Cu Kα radiation at 2θ ranging between 10° and 80° was employed to identify the crystal structure of samples. X-ray photoelectron spectroscopy (XPS, ESCALAB 250Xi) was used to investigate the surface property and chemical state of samples. Scanning electron microscopy (SEM, SU8010) and transmission electron microscopy (TEM, Talos-F200X) were used to confirm the morphology and structure of samples. The Raman spectra were performed using a confocal micro-Raman spectrometer (Thermo DXR2Xi Microscope, USA). UV-vis diffusion reflectance spectra (DRS) were analyzed on Lambda 950 spectrophotometer (PerkinElmer). The electron spin resonance (ESR) spectra were recorded on the EPR spectrometer (Bruker EMX plus). The FT-IR spectrometer (TENSOR27, AXS) was employed to investigate the *ex situ* Fourier transform infra-red spectroscopy. The Brunauer–Emmett–Teller specic surface area was estimated using the Microtrac BEL instrument. The photoluminescence (PL) spectra were recorded on a fluorescence spectrophotometer (FP-6500, Japan).

2.4 Photocatalytic activity tests

The photocatalytic performance of samples were evaluated by the degradation of RhB and CIP under the visible light (500 W Xe lamp, 420 nm $\leq \lambda$) and the simulated sunlight irradiation (500 W Xe lamp, $200 \leq \lambda \leq 800$ nm), respectively. The monochromatic light lamps (3 W) with the wavelength of 405, 550 and 630 nm were employed to investigate the photosensitization of RhB. A circulating water pump was used to keep the reaction temperature at 25 °C. Typically, 20 mg of photocatalyst was

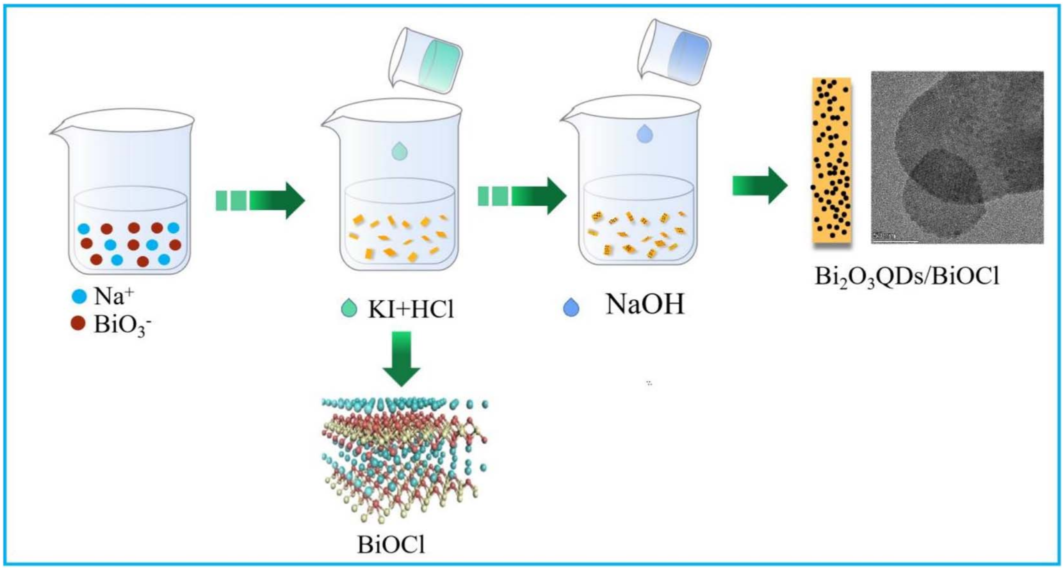

Scheme 1 The schematic diagram of Bi_2O_3QDs/BiOCl heterojunction preparation.

ultrasonically dispersed into 50 mL contaminant solution and then magnetically dispersed for 1 h in the darkness to reach the adsorption–desorption equilibrium. After turn on the light, 2.5 mL of suspension was gathered at given intervals and centrifuged to remove the particles. The concentration of contaminant was determined on the UV-vis spectrometer. The degradation efficiency was obtained through the following equation:

$$\text{Degradation efficiency }(\%) = \frac{C_0 - C_t}{C_0} \times 100\% \quad (1)$$

where C_0 and C_t represent the initial concentration and the temporal concentration of contaminant, respectively.

3. Results and discussion

3.1 Composition, morphology and structure of materials analysis

XRD was carried out to investigate the phase composition of materials, the results are shown in Fig. 1a. It can be seen that all the diffraction peaks of samples can be indexed to the tetragonal phase of BiOCl (JCPDS Card No. 82-485). The main diffraction peaks at 2 theta angles of 12.02°, 24.12°, 26°, 33.33°, 34°, 41°, 46.8°, 49.77°, 54.29° and 58.74° are indexed to the [001], [002], [101], [110], [001], [012], [112], [113], [211] and [212] plane of BiOCl, respectively.[31] The diffraction peaks of Bi_2O_3 cannot be observed in the spectrum of Bi_2O_3QDs/BiOCl heterojunction, which may be ascribed to the low content and small grain size of Bi_2O_3QDs.[32] In addition, the full width at half maximum (FWHM) of the diffraction peaks of the Bi_2O_3QDs/BiOCl heterojunction is larger than that of the pure BiOCl, suggesting the smaller grain size of Bi_2O_3QDs/BiOCl heterojunction.[33] It may be attributed to an increase in pH value of solution inhibiting the growth of BiOCl along the *c*-axis [001] orientations. Moreover, it is obvious that the value of $I_{[110]}/I_{[101]}$ of Bi_2O_3QDs/BiOCl heterojunction is higher than that of BiOCl, indicating the well growth direction along the [110] facet orientation.[34–36]

The Raman spectra of the samples were carried out to investigate the structural information and the incorporation of the Bi_2O_3QDs in the BiOCl (Fig. 1b). Three characteristic peaks at 65, 150 and 206 cm^{-1} can be found in both curves, which conform to the A_{1g} external, A_{1g} internal of Bi–Cl stretching mode and E_g internal of the stretching mode in BiOCl,[37] respectively. The relatively weak peak located at 401 cm^{-1} corresponding to the E_g and B_{1g} bands was generated by the motion of oxygen atoms. Comparing with the BiOCl, the peaks intensity of the Bi_2O_3QDs/BiOCl heterojunction significantly reduces after the introduction of Bi_2O_3QDs, demonstrating a strong interaction between the BiOCl and the Bi_2O_3QDs, which can increase electron density of the composites.[38]

Fig. 1c depicts the FT-IR spectra of BiOCl and Bi_2O_3QDs/BiOCl heterojunction. The peaks at 1620 cm^{-1} and 3450 cm^{-1} are assigned to the surface hydroxyl and the adsorbed water molecules. The absorption peak at 525 cm^{-1} belongs to the symmetrical A_{2u}-type vibration of Bi–O stretching mode in BiOCl structure. The peaks at 1060 cm^{-1} and 1450 cm^{-1} are attributed to the asymmetry stretching vibration of Bi–Cl bond of BiOCl species. It is worth on noting that comparing to the spectrum of BiOCl, there is a peak signal at 842 cm^{-1} in the Bi_2O_3QDs/BiOCl heterojunction (the enlarged image shown in Fig. 1d), which signifies the characteristic stretching vibration of Bi–O bond in Bi_2O_3 species,[39,40] suggesting the existence of Bi_2O_3. The results of the Raman and FT-IR reveal that the Bi_2O_3QDs/BiOCl heterojunction has been prepared successfully.

To explore the morphology, microstructure and element composition of the composites, the SEM, TEM and elemental color mapping were performed. As shown in Fig. 2a and b, the pure BiOCl exhibits the chufa-like features with a size of 1.2 μm in the diameter and 0.3–0.5 μm in the thickness (Fig. 2a).

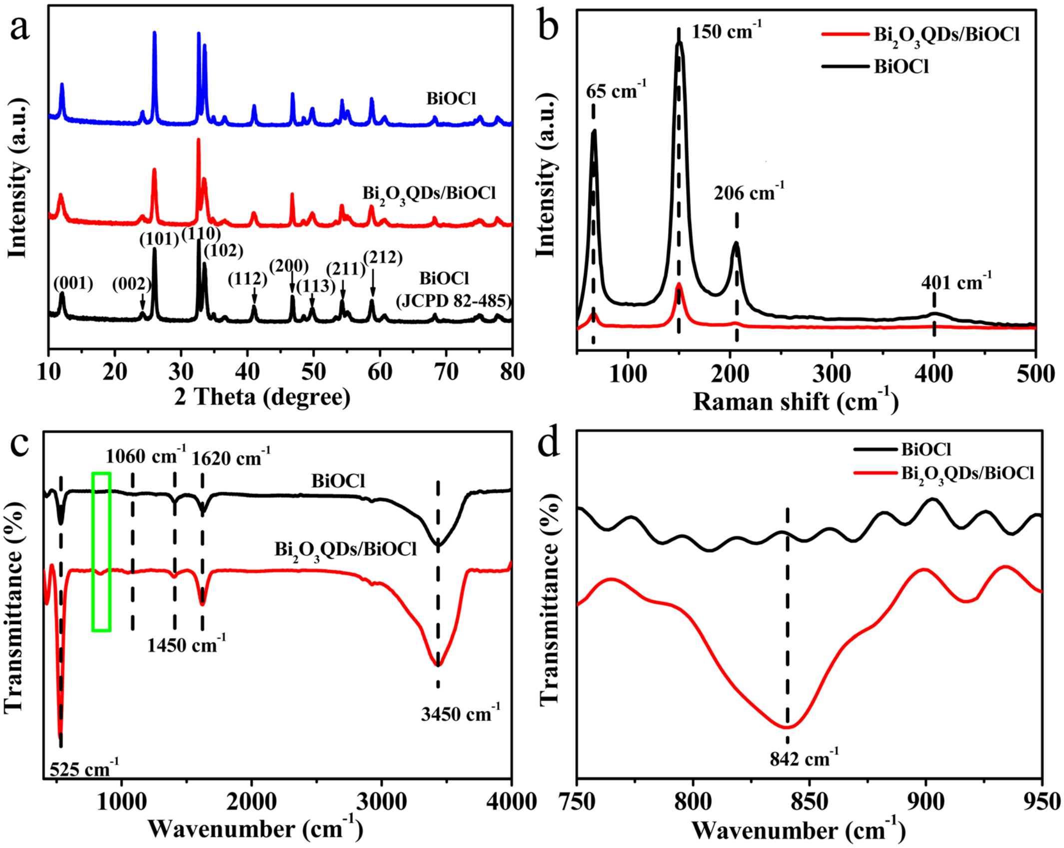

Fig. 1 (a) XRD patterns, (b) Raman spectra, (c) FT-IR spectrum of pure BiOCl and Bi_2O_3QDs/BiOCl heterojunction and (d) the corresponding FT-IR pattern from green rectangular box in the (c).

However, the Bi_2O_3QDs/BiOCl heterojunction (Fig. 2b) is mainly composed of the smaller square-like nanosheets with 100 nm in the width and 30 nm in the thickness, which could be ascribed to that the Bi_2O_3 phase is gradually formed as a nano-granular structure on the surface of the BiOCl, and alters the growth direction of the Bi_2O_3QDs/BiOCl heterojunction along from the initial [001] facets orientation to [110] facets orientation.[34] It is well consistent with the XRD analysis in Fig. 1a. In terms of the preparation process (Scheme 1) and the characterization data, a typical formation mechanism of Bi_2O_3QDs/BiOCl heterojunction is proposed. Firstly, the Bi^{5+} is reduced into the Bi^{3+} by the I^- (eqn (2)). Meanwhile, Bi^{3+} can be hydrolyzed to produce an intermediate $[Bi_2O_2]^{2+}$ (eqn (3)). Secondly, the $[Bi_2O_2]^{2+}$ will react with Cl^- to form the precipitant BiOCl due to the small solubility product constant ($K_{sp} = 1.8 \times 10^{-31}$) (eqn (4)).[41] Finally, the $[Bi_2O_2]^{2+}$ and OH^- produces the precipitant Bi_2O_3 when the pH of the solution is higher than 13.0 with adding sodium hydroxide (eqn (5)).[38]

$$BiO_3^- + 2I^- + 6H^+ \rightarrow Bi^{3+} + I_2 + 3H_2O \quad (2)$$

$$2Bi^{3+} + 2H_2O \rightarrow [Bi_2O_2]^{2+} + 4H^+ \quad (3)$$

$$[Bi_2O_2]^{2+} + 2Cl^- \rightarrow 2BiOCl\downarrow \quad (4)$$

$$[Bi_2O_2]^{2+} + 2OH^- \rightarrow Bi_2O_3\downarrow + H_2O \quad (5)$$

The TEM and HRTEM images in Fig. 2c–f can further demonstrate the morphology and structure of the samples. In Fig. 2c, the almost-transparent image reveals the ultrathin nanosheet structure of Bi_2O_3QDs/BiOCl heterojunction. Furthermore, it can be clearly seen that a lot of dense dots are uniformly distributed on the surface of the nanosheets (Fig. 2d and f). It can be observed by further high-resolution TEM image (Fig. 2e). The lattice fringes with the spacing of 0.272 nm and 0.322 nm are assigned to the BiOCl [110] and Bi_2O_3 [012] plane,[37] respectively. Moreover, the diameter of the uniformly distributed Bi_2O_3 quantum dots is about 8 nm. The continuity of the lattice fringes between Bi_2O_3QDs and BiOCl demonstrates an original connection and a strong coupling between the two phases, indicating the successfully hybridization of the Bi_2O_3QDs/BiOCl heterojunction. It will benefit the separation of the photo-induced electron–hole pairs to enhance the photocatalytic efficiency. In addition, the elemental mapping images (Fig. 2g–i) reveal that the Bi_2O_3QDs/BiOCl heterojunction only contains Bi, O and Cl elements, no other elements can be detected.

XPS was conducted to analyze the elemental composition and the surface chemical state of samples, the results are shown in Fig. 3. The survey spectrum of Bi_2O_3QDs/BiOCl heterojunction (Fig. 3a) reveals the presence of Bi, O and Cl elements

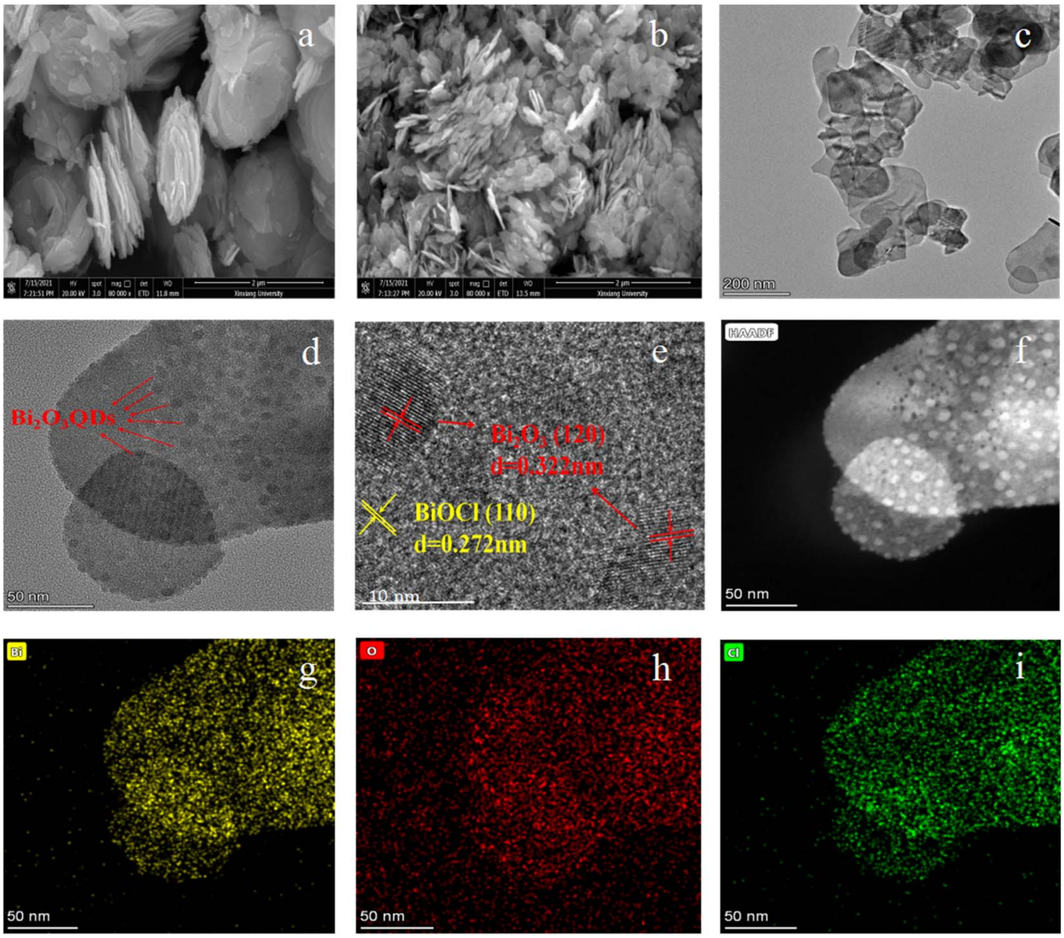

Fig. 2 SEM images of (a) BiOCl and (b) Bi_2O_3QDs/BiOCl heterojunction, (c–f) TEM and HRTEM images of Bi_2O_3QDs/BiOCl heterojunction, and (g–i) elemental color mapping of Bi, O and Cl.

with the binding energy peaks at 163.0 eV (Bi 4f), 442.0 eV (O 1s) and 198.0 eV (Cl 2p),[42] respectively. The peak of C 1s located at 283.0 eV is produced in the apparatus as calibration. Fig. 3b–d illustrate the high-resolution XPS spectra of Bi, O and Cl, respectively. In Fig. 3b, two peaks at 165.0 eV and 159.7 eV are corresponded to the Bi $4f_{5/2}$ and Bi $4f_{7/2}$, respectively, which are the characteristic peaks of Bi^{3+} ions in BiOCl material.[43] The banding energy of O 1s is located at 530.65 eV in Fig. 3c.[37] The XPS spectra of Cl element is displayed in Fig. 3d, it can be clearly observed that two strong bands located at 198.4 eV and 200.0 eV are assigned to the Cl $2p_{3/2}$ and Cl $2p_{1/2}$, respectively.[43] Meanwhile, comparing with the pure BiOCl, the spectra of Bi, O, Cl in Bi_2O_3QDs/BiOCl heterojunction show a little shift to the higher binding energy, which may be attributed to the following two aspects. Firstly, the hybridization of BiOCl and Bi_2O_3QDs results in the formation of an interfacial structure, which can change the chemical environment of the elements.[44] On the other hand, the coupling effects produced by the Bi_2O_3QDs/BiOCl heterojunction can increase electron density of the BiOCl.[45] The results of XPS analysis are consistent with that of the FT-IR and HRTEM, further revealing the formation of the Bi_2O_3QDs/BiOCl heterojunction.

The Fig. 4 illustrates pore size distribution curves and the N_2 adsorption–desorption isotherms of the BiOCl and Bi_2O_3QDs/BiOCl heterojunctions and the results were listed in Table 1. The average pore size of the BiOCl and Bi_2O_3QDs/BiOCl are 6.55 and 8.17 nm, respectively, which can be categorized as mesoporous material.[46] The N_2 adsorption–desorption isotherms of all composites appear a type IV isotherm through the IUPAC classification.[47] The specific surface areas are 7.163 and 17.497 $m^2 g^{-1}$ of the BiOCl and Bi_2O_3QDs/BiOCl, respectively. The increased surface area may ascribe to the loading of Bi_2O_3, which inhibit the aggregation of the BiOCl nanosheets. This phenomenon is consistent with the SEM result. Generally, the higher specific surface area and larger pore volume can provide more active sites and increase the photocatalytic performance.

3.2 Optical performance analysis

The UV-vis diffuse reflection spectroscopy was employed to study the optical absorption performance of materials. As shown in Fig. 5a, the maximal absorbance edge of BiOCl is located at 357 nm in UV region. In contrast, the absorption edge of the Bi_2O_3QDs/BiOCl heterojunction enlarges a little to

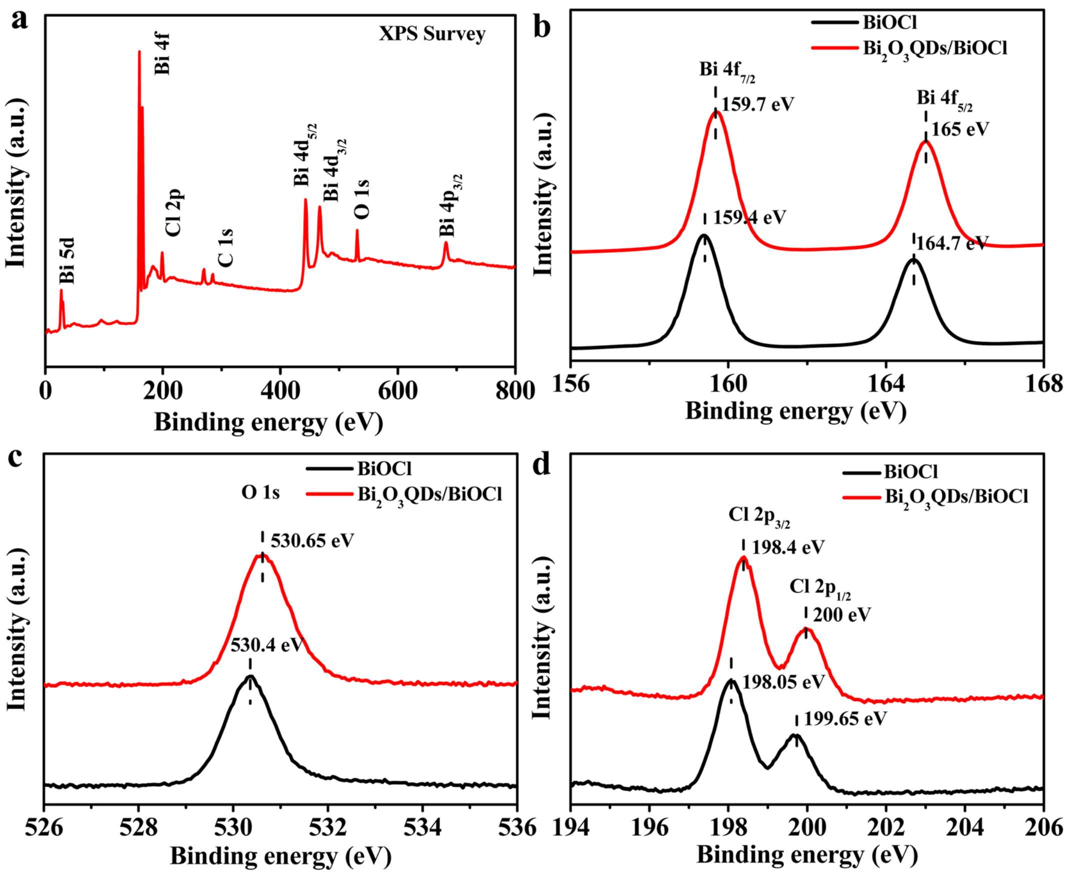

Fig. 3 XPS spectra of BiOCl and Bi_2O_3QDs/BiOCl: survey spectrum (a), high resolution XPS spectra of Bi 4f (b), O 1s (c), Cl 2p (d).

364 nm, which may be due to the introduction of Bi_2O_3QDs owning the visible-light response. In addition, the Bi_2O_3QDs/BiOCl heterojunction has the lower absorption in the region of 360–420 nm compared to the BiOCl.

The band-gap energy is obtained though the Kubelka–Munk function according to the equation as below:[48]

$$ahv = A(hv - E_g)^{1/2} \qquad (6)$$

Table 1 Summary of specific surface area and pore size of BiOCl and Bi_2O_3QDs/BiOCl

Sample	Specific surface area (m^2 g^{-1})	Average pore size (nm)
BiOCl	7.163	6.55
Bi_2O_3QDs/BiOCl	17.497	8.17

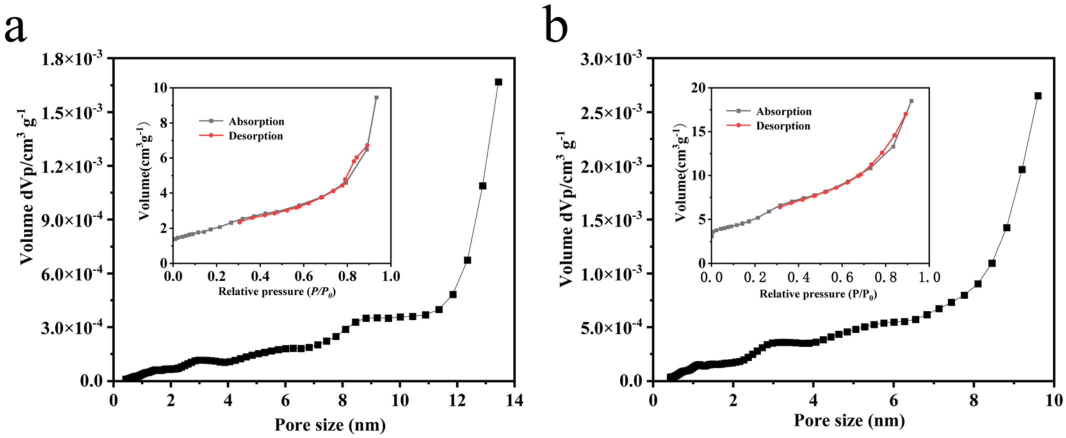

Fig. 4 (a) and (b) pore size distributions and N_2 adsorption–desorption isotherms (inset) of BiOCl and Bi_2O_3QDs/BiOCl.

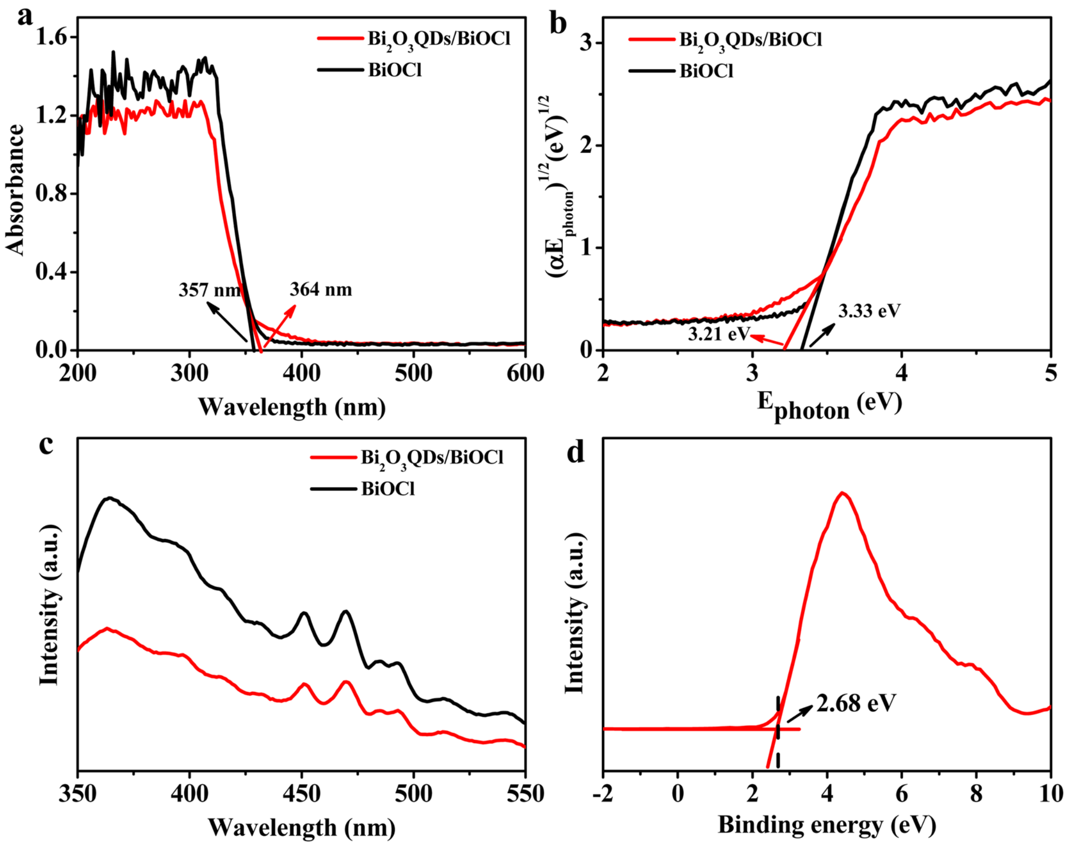

Fig. 5 (a) UV-vis absorption spectra, (b) plots of $(ahv)^{1/2}$ *versus hv*, (c) PL spectra, (d) valence band XPS spectra of BiOCl.

where *a* stands for the absorption coefficient, *hv* is the incident photon energy, *A* is a constant, and E_g represents the band gap energy. As shown in Fig. 5b, the band gap of Bi_2O_3QDs/BiOCl heterojunction and the pure BiOCl are estimated to be 3.21 eV and 3.33 eV. It means that the heterojunction possesses the higher utilization efficiency of light and the better separation of electron–hole pairs.

The photoluminescence spectra reflect the optical performance of the semiconductor catalyst and correlate with the recombination rate of the electrons and holes. The stronger fluorescence intensity is generally accompanied by the higher recombination rate.[49] Fig. 5c shows the PL spectra of Bi_2O_3QDs/BiOCl and BiOCl samples with an excitation wavelength of 330 nm. It can be seen that the fluorescence intensity of the Bi_2O_3QDs/BiOCl heterojunction is significantly lower than that of the pure BiOCl, suggesting that the Bi_2O_3QDs/BiOCl heterojunction can effectively inhibit the recombination of the photogenerated electrons and holes. In addition, Fig. 5d shows the valence band XPS spectra of BiOCl around 2.68 eV, which will provide the important data support for the subsequent mechanism analysis.

3.3 Photocatalysis performance study

The photocatalytic performance evaluation of the samples is shown in Fig. 6. The degradation of RhB self-photosensitization almost can be ignored in the absence of the photocatalysts. It can be clearly seen that the catalytic degradation performance of two samples is significantly different. The degradation rate of RhB is 63.7% and 93.7% over the BiOCl and the Bi_2O_3QDs/BiOCl heterojunction under visible light irradiation for 30 min, respectively. For the colorless CIP antibiotics (Fig. 6b), the photocatalytic degradation efficiency of the BiOCl and the Bi_2O_3QDs/BiOCl heterojunction are 46% and 87.1% under the simulated sunlight irradiation for 5 h, respectively. Compared with the pure BiOCl, the photocatalytic performance of the Bi_2O_3QDs/BiOCl heterojunction for the degradation on the RhB and the CIP are significantly improved by 30% and 40%, respectively.

Langmuir–Hinshelwood model is conducted to estimate the degradation rate.[24] The calculation formula is as following:

$$-\ln\frac{C_t}{C_0} = kt \tag{7}$$

where *k* is the reaction rate constant obtained from the slope of the straight line, C_0 and C_t represent the initial absorbance and the temporal absorbance of contaminant at *t* time, respectively. In Fig. 6c, the photocatalytic degradation reactions conform to the pseudo-first-order kinetics. For the degradation of RhB, the *k* value (Fig. 6c) of the Bi_2O_3QDs/BiOCl heterojunction is 0.0847 min^{-1}, which is as 2.54 folds as BiOCl (0.0333 min^{-1}). From Fig. 6d, the *k* value of Bi_2O_3QDs/BiOCl heterojunction can reach 0.2739 h^{-1}, which is as 2.38 times as the BiOCl. The excellent photodegradation activity of the Bi_2O_3QDs/BiOCl heterojunction can be attributed to the factors as follow. On

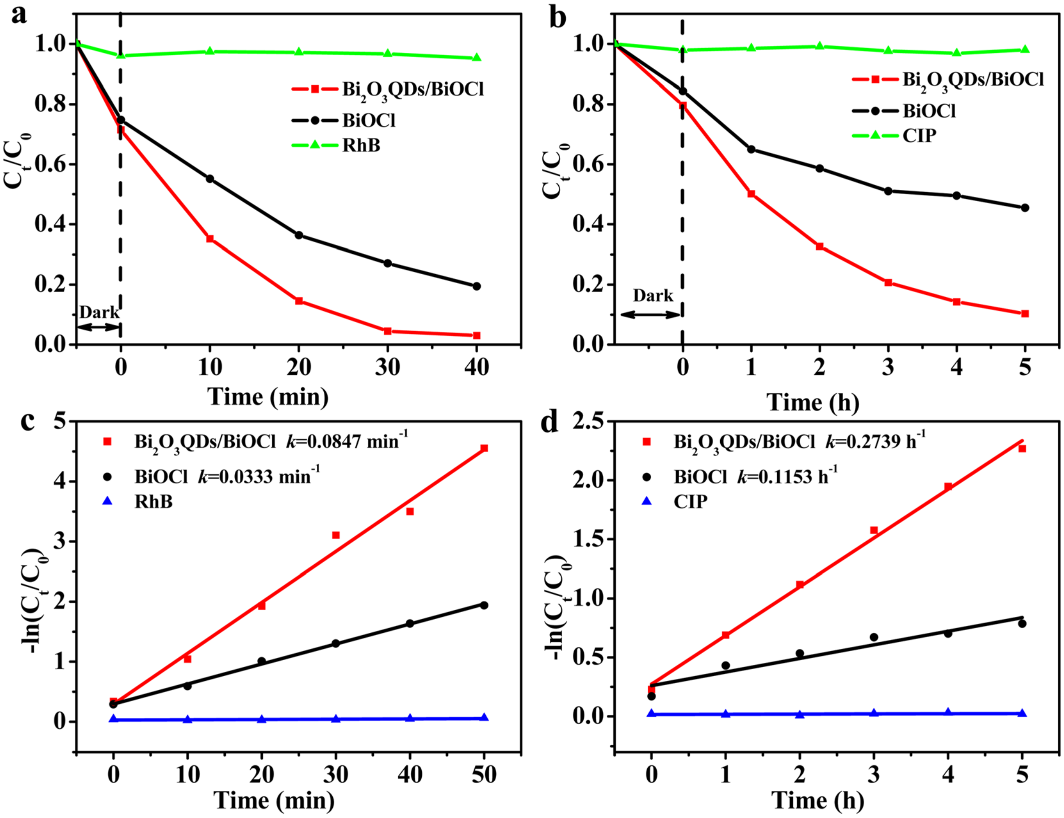

Fig. 6 (a) and (b) photodegradation of RhB and CIP, (c) and (d) the curves of ln(C_t/C_0) *versus* time for photodegradation on the RhB and the CIP.

the one hand, the Bi_2O_3QDs/BiOCl nanosheets possess the smaller grain size and thickness comparing to the pure BiOCl, which supplies the higher specific area and more active plots to enhance the transfer of electrons to the surface. On the other hand, the unique heterostructure can accelerate the transfer of electrons and restrict the recombination of photogenerated electrons and holes according to the PL results in Fig. 5c.

Interestingly, Bi_2O_3QDs/BiOCl heterojunction also exhibits the visible-light activity for the RhB decomposition, which may due to the dye photosensitization effect of the RhB.[50] Therefore, the monochromatic light lamps with the wavelength of 405, 550 and 630 nm were employed to investigate the photosensitization effect in the photocatalytic degradation of RhB. As shown in Fig. 7a and b, both the Bi_2O_3QDs/BiOCl heterojunction and BiOCl exhibit the photocatalytic performance on RhB under the three kinds of monochromatic light irradiation. Particularly, the Bi_2O_3QDs/BiOCl heterojunction show outstanding photocatalytic activity comparing to the pure BiOCl under the light with the wavelength of 550 and 630 nm. However, only about 79.1% and 46% of CIP can be degraded under monochromatic light irradiation of 405 nm over the Bi_2O_3QDs/BiOCl heterojunction and the BiOCl, respectively. There is almost no degradation of CIP under the monochromatic light irradiation of 550 nm and 630 nm (Fig. 7c and d). Combining with the above results, it can be concluded that the enhancement of visible light activity of BiOCl in the process of degrading RhB is primarily attributed to the dye photosensitization effect. For the Bi_2O_3QDs/BiOCl heterojunction, it is the combination of photosensitization effect and heterojunction effect that render the Bi_2O_3QDs/BiOCl heterojunction have an outstanding visible photocatalytic performance in the process of degrading RhB.

To further define the stability of the Bi_2O_3QDs/BiOCl heterojunction, the cycling experiments for mineralizing RhB were conducted. As shown in Fig. 8, the photocatalytic degradation rate of Bi_2O_3QDs/BiOCl on RhB still remains at above 90% after four cycles, indicating its outstanding photocatalytic durability.

3.4 Proposal of photocatalytic mechanism

In order to further verify the active species in the photocatalytic process, the trapping experiments were carried out by adding three trapping agents in RhB solution, such as EDTA-2Na for holes (h^+), benzoquinone (BQ) for superoxide radicals ($^{\bullet}O_2^-$) and *tert*-butyl alcohol (TBA) for hydroxyl radicals ($^{\bullet}OH$).[51] The results are illustrated in Fig. 9b. For Bi_2O_3QDs/BiOCl heterojunction, the addition of TBA and BQ has a slightly influence on the photocatalytic activity, indicating that $^{\bullet}O_2^-$ and $^{\bullet}OH$ are not main active species in the photodegradation of RhB. When the EDTA-2Na is added into the RhB solution, the photocatalytic activity is significantly decreased from 99% to 40.5%, implying that the holes play a key role on the photocatalytic process. This result is exactly corresponding to the above mechanism analysis. Therefore, the formation of Bi_2O_3QDs/BiOCl heterojunction can significantly improve the separation efficiency of

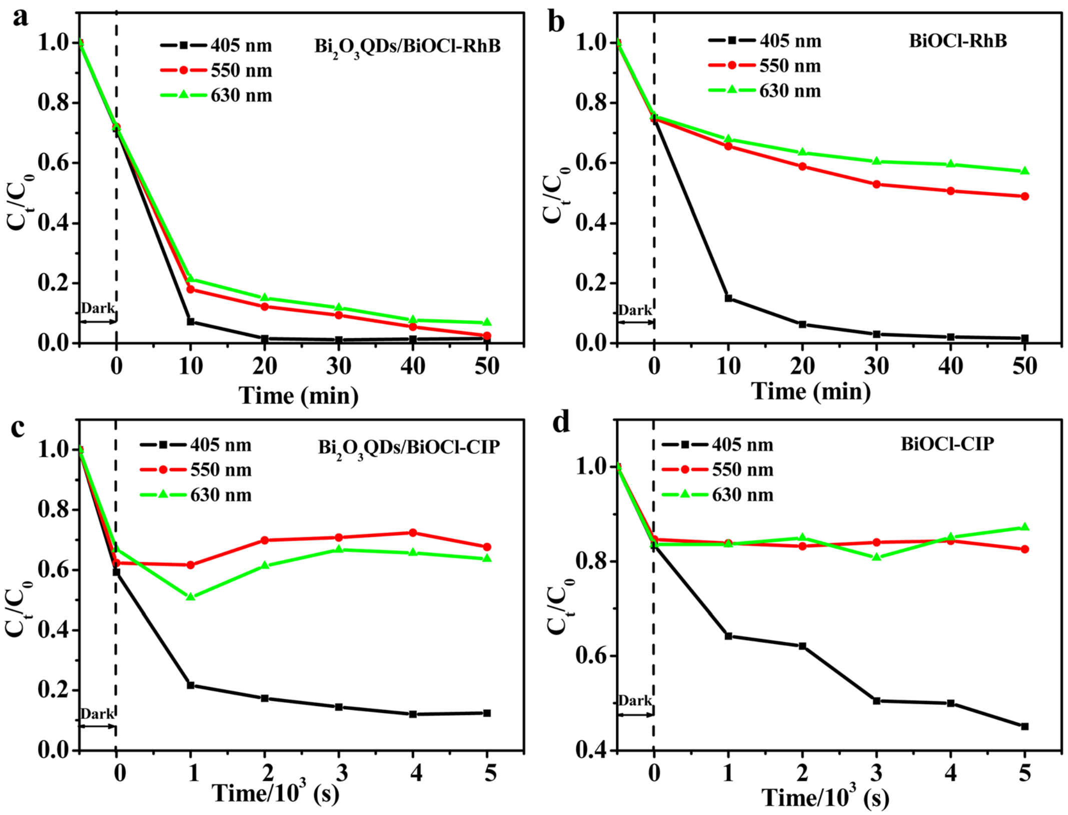

Fig. 7 The monochromatic photodegradation testing of RhB (a and b) and CIP (c and d) over Bi_2O_3QDs/BiOCl and BiOCl, respectively.

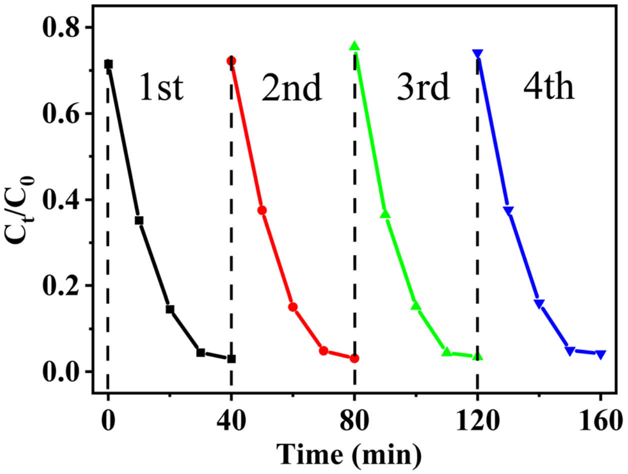

Fig. 8 Cycle runs during the photocatalytic degradation of RhB.

the photo-induced charge carriers and effectively enhance the photocatalytic activity.

To further confirm the separation efficiency and transfer mechanism of photo-induced electron for the Bi_2O_3QDs/BiOCl heterojunction, the ESR testing using the 5,5-dimethyl-1-pyrroline-*N*-oxide (DMPO) were performed under dark and light irradiation of 5 min and 10 min, respectively. As displayed in Fig. 9b, no characteristic peaks can be seen when the testing of the DMPO was conducted under dark conditions. Subsequently, when the solution of the BiOCl was illuminated by xenon lamp, six distinct characteristic peaks can be observed, indicating that the photo-induced electrons start to generate and combine with oxygen to produce $^{\bullet}O_2^-$. Nevertheless, there is almost no apparent characteristic peak in the ESR spectra of the Bi_2O_3QDs/BiOCl heterojunction under dark conditions and illumination. In Fig. 9c, it reveals that the Bi_2O_3QDs/BiOCl heterojunctions possess high separation efficiency of photo-induced carriers. The electrons are transferred from the lower valence band of BiOCl to the higher that of the Bi_2O_3. The accumulated electrons in the CB ($E_{CB} = 0.33$ eV) of Bi_2O_3 cannot reduce O_2 to the superoxide radicals ($^{\bullet}O_2^-$) due to the low redox potential of $O_2/^{\bullet}O_2^-$ (−0.046 eV/NHE), resulting in the disappearance of superoxide radicals in the ESR spectra (Fig. 9d). The above facts demonstrate that the charge transfer mechanism of the Bi_2O_3QDs/BiOCl heterojunction conforms to the type II charge transfer route rather than the Z-scheme carrier migration mechanism.

It has been confirmed by the above results that Bi_2O_3QDs/BiOCl heterojunction is favorable for the generation and separation of photo-induced electron–hole pairs. It is well known that the charge separation ability of the heterojunction semiconductors is jointly determined by the band edge potentials of each semiconductor.[52] Hence, the relative position of band alignment between the Bi_2O_3 and the BiOCl makes a great impact on the photocatalytic performance of the Bi_2O_3QDs/BiOCl heterojunction. From Fig. 5b and d, the valence band potential (E_{VB})

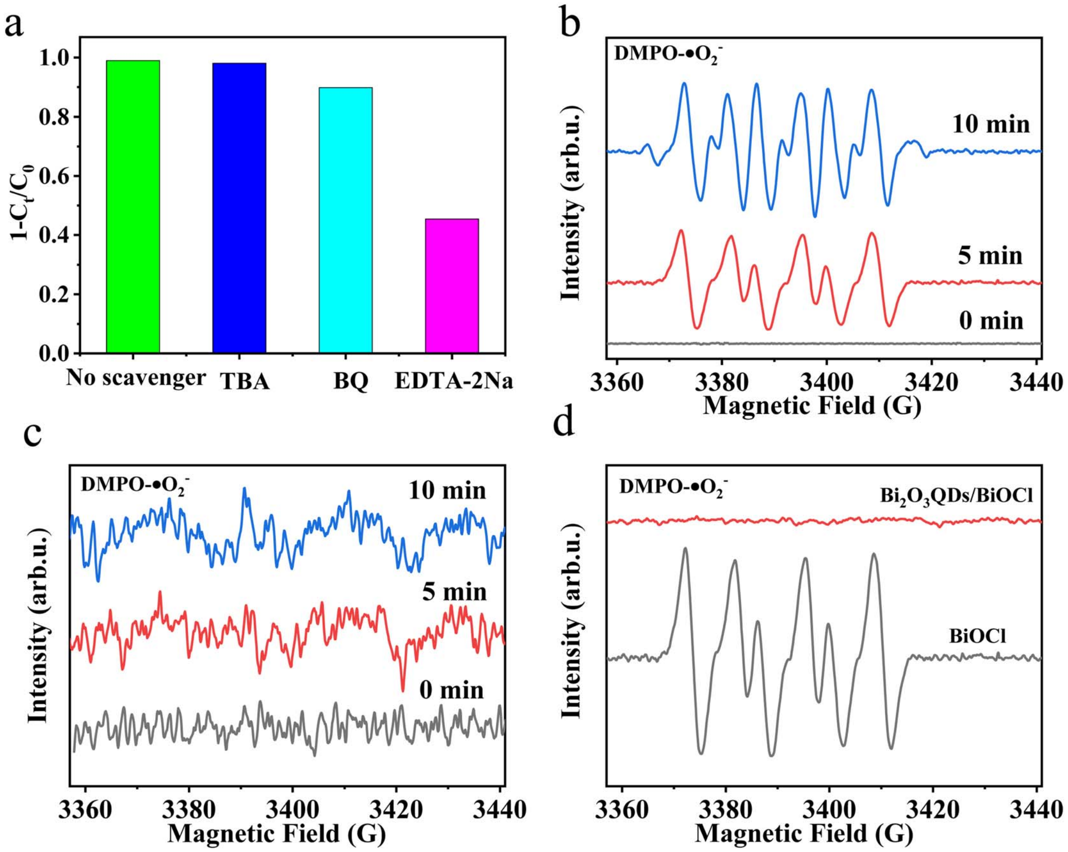

Fig. 9 (a) Scavenger experiments, (b and c) ESR spectra of BiOCl and Bi_2O_3QDs/BiOCl under illumination, respectively, (d) ESR spectra of DMPO-O_2^- after 5 min of light irradiation.

and the E_g of the BiOCl are measured to be 2.68 eV and 3.33 eV, respectively. The conduction band potential (E_{CB}) is calculated to be −0.65 eV by the formula: $E_{CB} = E_{VB} - E_g$.[52] The E_{VB} and E_{CB} of Bi_2O_3 are 3.13 eV and 0.33 eV obtained from the reported literature,[33] respectively. The schematic band diagrams of the Bi_2O_3QDs/BiOCl heterojunction are presented in Fig. 10. The internal electric field at the interface between BiOCl and Bi_2O_3-QDs can drive the electrons to the higher conduction band (CB)

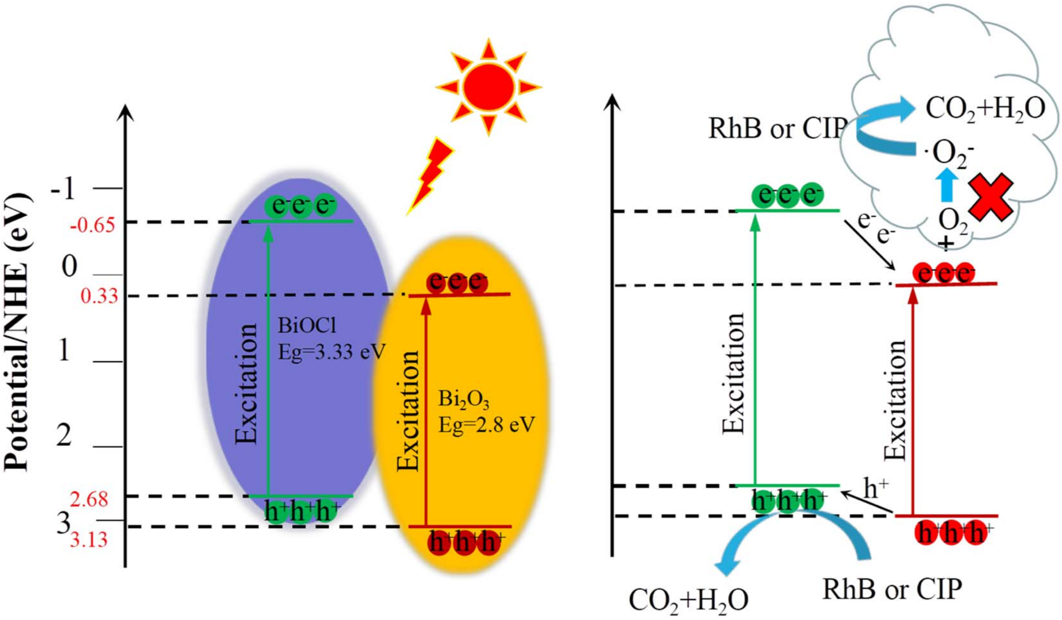

Fig. 10 Possible photocatalytic mechanism of the Bi_2O_3QDs/BiOCl heterojunction.

and make the holes to the lower value band (VB).[49] Therefore, when excited by light, the photogenerated electrons in the CB of BiOCl could be transferred to the CB of Bi_2O_3QDs, and the holes in the VB of the Bi_2O_3QDs can be transferred to the VB of the BiOCl. The accumulated electrons in the CB ($E_{CB} = 0.33$ eV) of Bi_2O_3QDs cannot reduce O_2 to the superoxide radicals ($^{\bullet}O_2^-$).[51] The holes in the VB ($E_{VB} = 3.13$ eV) of the Bi_2O_3QDs can oxidize OH^- into hydroxyl radicals ($^{\bullet}OH$) (2.38 eV/NHE).[51] In this way, the photo-induced carriers of the catalysts are effectively separated and the strong photocatalytic redox ability are retained in the heterojunction to degrade the pollutants.

4. Conclusions

In conclusion, the Bi_2O_3QDs/BiOCl heterojunction has been successfully prepared *via* a facile one-step *in situ* chemical deposition method. The Bi_2O_3 quantum dots with the size of about 8 nm are uniformly distributed on the surface of the BiOCl. The SEM and BET observations of the composites show that the Bi_2O_3QDs/BiOCl heterojunction possesses the smaller grain size, the higher specific area and more active sites compared with the pure BiOCl nanosheets. The heterojunction exhibits the enhanced photocatalytic activity for the degradation of RhB and CIP, which are as 2.54 and 2.38 times as that of the pure BiOCl, respectively. The photosensitization effect is investigated by monochromatic photodegradation. The photocatalytic mechanism of the Bi_2O_3QDs/BiOCl heterojunction has been also proposed in detail. In addition, the radical trapping tests demonstrate that the holes are the dominating active species. The ESR tests demonstrate that the charge transfer mechanism of the Bi_2O_3QDs/BiOCl heterojunction conforms to the type II charge transfer route. The facile preparation process and excellent reusability endow the Bi_2O_3QDs/BiOCl heterojunction prospective for application in wastewater treatment. Simultaneously, this work provides a new idea on exploitation and synthesis of BiOCl-based materials with high-photocatalytic performance.

Conflicts of interest

There are no conflicts to declare.

Acknowledgements

The financial support from National Natural Science Foundation of China (NSFC, No. 51872131, 51672118 and 51972156) and the Distinguished Professor Project of Education Department of Liaoning are acknowledged.

References

1 A. Hassan, S. Z. Ilyas, A. Jalil and U. Zahid, Monetization of the environmental damage caused by fossil fuels, *Environ. Sci. Pollut. Res.*, 2021, **28**, 21204–21211.

2 M. A. Koondhar, Z. X. Tan, G. M. Alam, Z. A. Khan, L. W. Wang and R. Kong, Bioenergy consumption, carbon emissions, and agricultural bioeconomic growth: a systematic approach to carbon neutrality in China, *J. Environ. Manage.*, 2021, **296**, 113242.

3 O. Y. Hao, H. Q. Huang, H. G. Wang and X. M. Zheng, The morphology evolution of nitrogen-doped carbon quantum dots/hollow TiO_2 composites and their applications in photocatalysis, *J. Mater. Sci.*, 2020, **55**, 1–14.

4 Y. M. Wang, X. X. Liu, L. Q. Shang, S. S. Ge, G. Song, N. Naik, Q. Shao, J. Lin and Z. H. Guo, Metal organic framework-derived C-doped ZnO/TiO_2 nanocomposite catalysts for enhanced photodegradation of Rhodamine B, *J. Colloid Interface Sci.*, 2021, **599**, 566–576.

5 F. J. Duan, C. C. Liu, X. C. Liu, L. L. Wang, S. Zhang and X. B. Liu, TiO_2 immobilized on polyarylene ether nitrile/Fe^{3+} complex for efficient adsorption and photocatalytic degradation towards methylene blue, *J. Alloys Compd.*, 2021, **875**, 159951.

6 C. T. Zhang, L. Wang, F. X. Yuan, R. Meng, J. Chen, W. H. Hou and H. J. Zhu, Construction of p–n type Ag_3PO_4/$CdWO_4$ heterojunction photocatalyst for visible-light-induced dye degradation, *Appl. Surf. Sci.*, 2020, **534**, 147544.

7 Z. F. Shen, F. F. Li, J. R. Lu, Z. D. Wang, R. Li, X. C. Zhang, C. M. Zhang, Y. W. Wang, Y. F. Wang, Z. P. Lv, J. X. Liu and C. M. Fan, Enhanced N_2 photofixation activity of flower-like BiOCl by in situ Fe(III) doped as an activation center, *J. Colloid Interface Sci.*, 2021, **584**, 174–181.

8 H. L. Qin, Y. S. Zhang, S. J. He, Z. Y. Guan, Y. T. Shi, X. Y. Xie, D. S. Xia, D. Y. Li and H. M. Xu, Increasing the migration and separation efficiencies of photogenerated carriers in CQDs/BiOCl through the point discharge effect, *Appl. Surf. Sci.*, 2021, **562**, 150214.

9 Q. Su, L. L. Zhu, M. R. Zhang, Y. Li, S. Y. Liu, J. Y. Lin, F. Song, W. Zhang, S. M. Zhu and J. Pan, Construction of a bioinspired hierarchical $BiVO_4$/BiOCl heterojunction and its enhanced photocatalytic activity for phenol degradation, *ACS Appl. Mater. Interfaces*, 2021, **13**, 32906–32915.

10 T. Shen, X. K. Shi, J. X. Guo, J. Li and S. D. Yuan, Photocatalytic removal of NO by light-driven Mn_3O_4/BiOCl heterojunction photocatalyst: optimization and mechanism, *Chem. Eng. J.*, 2021, **408**, 128014.

11 Q. Zhou, W. Y. Huang, C. Xu, X. Liu, K. Yang, D. Li, Y. Hou and D. D. Dionysiou, Novel hierarchical carbon quantum dots-decorated BiOCl nanosheet/carbonized eggshell membrane composites for improved removal of organic contaminants from water via synergistic adsorption and photocatalysis, *Chem. Eng. J.*, 2021, **420**, 129582.

12 C. Liu, Y. H. Ren, Z. W. Wang, Y. Z. Shi, B. B. Guo, Y. Yu and L. Wu, Flower-like BiOCl nanospheres fabricated by an in situ self-assembly strategy for efficiently enhancing photocatalysis, *J. Colloid Interface Sci.*, 2022, **607**, 423–430.

13 Y. Q. Zhang, K. F. Zhao, J. T. Huang, H. Y. Hsu, J. W. Xu, R. Luque, W. X. Niu and G. B. Xu, Non-centrosymmetric hollow BiOCl nanocaps with tailored openings for the photocatalytic degradation of rhodamine B, *ACS Appl. Nano Mater.*, 2022, **5**, 2326–2334.

14 Z. P. Ma, L. N. Zhang, X. Ma and F. N. Shi, A dual strategy for synthesizing crystal plane/defect co-modified BiOCl

microsphere and photodegradation mechanism insights, *J. Colloid Interface Sci.*, 2022, **617**, 73–83.

15 X. Wang, J. Q. Zhu, X. H. Fu, J. G. Xu, X. Yu, Y. Zhu, Y. M. Zhang and M. S. Zhu, Boosted visible-light photocatalytic performance of Au/BiOCl/BiOI by high-speed spatial electron transfer channel, *J. Alloys Compd.*, 2021, **890**, 161736.

16 C. Y. Chen, T. Jiang, J. H. Hou, T. T. Zhang, G. S. Zhang, Y. C. Zhang and X. Z. Wang, Oxygen vacancies induced narrow band gap of BiOCl for efficient visible-light catalytic performance from double radicals, *J. Mater. Sci. Technol.*, 2022, **114**, 240–248.

17 J. Y. Cao, W. L. Cen, Y. Jing, Z. X. Du, W. Chua and J. J. Li, P-doped BiOCl for visible light photodegradation of tetracycline: an insight from experiment and calculation, *Chem. Eng. J.*, 2022, **435**, 134683.

18 C. Y. Wang, Y. J. Zhang, W. K. Wang, D. N. Pei, G. X. Huang, J. J. Chen, X. Zhang and H. Q. Yu, Enhanced photocatalytic degradation of bisphenol A by Co-doped BiOCl nanosheets under visible light irradiation, *Appl. Catal., B*, 2018, **221**, 320–328.

19 J. Liu, Y. P. Li, L. Y. Huang, C. B. Wang, L. Yang, J. W. Liu, C. Y. Huang and Y. H. Song, Fabrication of novel narrow/wide band gap $Bi_4O_5I_2$/BiOCl heterojunction with high antibacterial and degradation efficiency under LED and sunlight, *Appl. Surf. Sci.*, 2021, **267**, 150713.

20 L. B. Mao, H. Liu, L. L. Yao, W. Wen, M. M. Chen, X. H. Zhang and S. F. Wang, Construction of a dual-functional CuO/BiOCl heterojunction for high-efficiently photoelectrochemical biosensing and photoelectrocatalytic degradation of aflatoxin B1, *Chem. Eng. J.*, 2022, **429**, 132297.

21 Y. Lu, J. M. Song, W. F. Li, Y. L. Pan, H. Y. Fang, X. L. Wang and G. Hu, Preparation of BiOCl/Bi_2S_3 composites by simple ion exchange method for highly efficient photocatalytic reduction of Cr^{6+}, *Appl. Surf. Sci.*, 2020, **506**, 145000.

22 S. Y. Chai, Y. J. Kim, M. H. Jung, A. K. Chakraborty, D. Jung and W. I. Lee, Heterojunctioned BiOCl/Bi_2O_3, a new visible light photocatalyst, *J. Catal.*, 2009, **262**, 144–149.

23 F. Deng, Q. Zhang, L. X. Yang, X. B. Luo, A. J. Wang, S. L. Luo and D. D. Dionysiou, Visible-light-responsive graphene-functionalized Bi-bridge Z-scheme black BiOCl/Bi_2O_3 heterojunction with oxygen vacancy and multiple charge transfer channels for efficient photocatalytic degradation of 2-nitrophenol and industrial wastewater treatment, *Appl. Catal., B*, 2018, **238**, 61–69.

24 Q. H. Zhao, X. Y. Liu, Y. X. Xing, Z. L. Liu and C. F. Du, Synthesizing Bi_2O_3/BiOCl heterojunctions by partial conversion of BiOCl, *J. Mater. Sci.*, 2016, **52**(4), 2117–2130.

25 D. G. Teng, J. Qu, P. Li, P. Jin, J. Zhang, Y. Zhang and Y. J. Cao, Heterostructured α-Bi_2O_3/BiOCl nanosheet for photocatalytic applications, *Nanomaterials*, 2022, **12**(20), 3631.

26 S. L. Kong, Z. H. An, W. W. Zhang, Z. H. An, M. Yuan and D. H. Chen, Preparation of hollow flower-like microspherical β-Bi_2O_3/BiOCl heterojunction and high photocatalytic property for tetracycline hydrochloride degradation, *Nanomaterials*, 2020, **10**(1), 57.

27 A. L. Ruiz-Castillo, M. Hinojosa-Reyes, R. Camposeco-Solis and F. Ruiz, Photocatalytic activity of Bi_2O_3/BiOCl heterojunctions under uv and visible light illumination for degradation of caffeine, *Top. Catal.*, 2022, **65**, 1071–1087.

28 K. R. Nemade and S. A. Waghuley, LPG sensing application of graphene/Bi_2O_3 quantum dots composites, *Solid State Sci.*, 2013, **22**, 27–32.

29 C. D. Lv, G. Chen, J. X. Sun, C. S. Yan, H. J. Dong and C. M. Li, One-dimensional Bi_2O_3QD-decorated $BiVO_4$ nanofibers: electrospinning synthesis, phase separation mechanism and enhanced photocatalytic performance, *RSC Adv.*, 2015, **5**, 3767–3773.

30 B. H. Lou, C. L. Chen, J. J. Liu, S. H. Zou, L. P. Xiao and J. Fan, Selectively depositing Bi_2O_3 quantum dots on TiO_2 nanotubes for efficient visible-light-driven photocatalysis, *Mater. Lett.*, 2021, **288**, 129413.

31 X. D. Tang, C. S. Ma, N. Liu, C. L. Liu and S. L. Liu, Visible light β-Bi_2O_3/BiOCl heterojunction photocatalyst with highly enhanced photocatalytic activity, *Chem. Phys. Lett.*, 2018, **709**, 82–87.

32 F. F. Duo, Y. W. Wang, C. M. Fan, X. C. Zhang and Y. F. Wang, Enhanced visible light photocatalytic activity and stability of CQDs/BiOBr composites: the upconversion effect of CQDs, *J. Alloys Compd.*, 2016, **685**, 34–41.

33 J. J. Hu, G. Q. Xu, J. W. Wang, J. Lv, X. Y. Zhang, T. Xie, Z. X. Zheng and Y. C. Wu, Photocatalytic property of a Bi_2O_3 nanoparticle modified BiOCl composite with a nanolayered hierarchical structure synthesized by in situ reactions, *Dalton Trans.*, 2015, **44**, 5386–5395.

34 P. Intaphong1, A. Phuruangrat, T. Thongtem and S. Thongtem, Effect of pH on phase, morphologies, and photocatalytic properties of BiOCl synthesized by hydrothermal method, *J. Aust. Ceram. Soc.*, 2020, **56**, 41–48.

35 Z. W. Zou, H. M. Xu, D. Y. Li, J. Y. Sun and D. S. Xia, Facile preparation and photocatalytic activity of oxygen vacancy rich BiOCl with {001} exposed reactive facets, *Appl. Surf. Sci.*, 2019, **463**, 1011–1018.

36 X. Y. Wang, X. M. Liu, G. Liu, C. H. Zhang, G. Liu, S. C. Xu, P. Cui and D. Y. Li, Rapid synthesis of BiOCl graded microspheres with highly exposed (110) facets and oxygen vacancies at room temperature to enhance visible light photocatalytic activity, *Catal. Commun.*, 2019, **130**, 105769.

37 F. Deng, Q. Zhang, L. X. Yang, X. B. Luo, A. J. Wang, S. L. Luo and D. D. Dionysiou, Visible-light-responsive graphene-functionalized Bi-bridge Z-scheme black BiOCl/Bi_2O_3 heterojunction with oxygen vacancy and multiple charge transfer channels for efficient photocatalytic degradation of 2-nitrophenol and industrial wastewater treatment, *Appl. Catal., B*, 2018, **238**, 61–69.

38 M. Malligavathy and D. P. Padiyan, Phase purity analysis and optical studies of Bi_2O_3 nanoparticles suitable for photocatalytic activity, *Int. J. Nanosci.*, 2017, **16**, 1760040.

39 K. K. Bera, R. Majumdar, M. Chakraborty and S. K. Bhattacharya, Phase control synthesis of α, β and α/β Bi_2O_3 hetero-junction with enhanced and synergistic photocatalytic activity on degradation of toxic dye,

rhodamine-B under natural sunlight, *J. Hazard. Mater.*, 2018, **352**, 182–191.

40 S. P. S. David, S. Veeralakshmi, J. Sandhya, S. Nehru and S. Kalaiselvam, Room temperature operatable high sensitive toluene gas sensor using chemiresistive Ag/Bi_2O_3 nanocomposite, *Sens. Actuators, B*, 2020, **320**, 128410.

41 Y. Myung, F. Wu, S. Banerjee, J. Park and P. Banerjee, Electrical conductivity of p-type BiOCl nanosheets, *Chem. Commun.*, 2015, **51**, 2629–2632.

42 J. Y. Cao, Y. Jing, Z. X. Du, W. Chu, J. J. Li and W. L. Cen, WC/BiOCl binary composite photocatalyst for accelerating interfacial charge separation and sulfamethoxazole degradation, *Appl. Surf. Sci.*, 2021, **570**, 151201.

43 K. Wu, Z. G. Qin, X. S. Zhang, R. C. Guo, X. Z. Ren and X. P. Pu, Z-scheme BiOCl/Bi-Bi_2O_3 heterojunction with oxygen vacancy for excellent degradation performance of antibiotics and dyes, *J. Mater. Sci.*, 2020, **55**, 4017–4029.

44 H. W. Huang, Y. He, X. W. Li, M. Li, C. Zeng, F. Dong, X. Du, T. R. Zhang and Y. H. Zhang, $Bi_2O_2(OH)(NO_3)$ as a desirable $[Bi_2O_2]^{2+}$ layered photocatalyst: strong intrinsic polarity, rational band structure and {001} active facets co-beneficial for robust photooxidation capability, *J. Mater. Chem. A*, 2015, **3**, 24547–24556.

45 L. Hao, P. Ju, Y. Zhang, X. F. Zhai, C. J. Sun, J. Z. Duan, Y. Su, Z. X. Lu and D. K. Liao, Fabrication of hierarchical flower-like BiOI/MoS_2 heterostructures with highly enhanced visible-light photocatalytic activities, *Colloids Surf., A*, 2021, **610**, 125714.

46 Y. Y. Jiao, Q. Z. Huang, J. S. Wang, Z. H. He and Z. J. Li, A novel MoS_2 quantum dots (QDs) decorated Z-scheme g-C_3N_4 nanosheet/N-doped carbon dots heterostructure photocatalyst for photocatalytic hydrogen evolution, *Appl. Catal., B*, 2019, **247**, 124–132.

47 L. L. Chu, J. Zhang, Z. S. Wu, C. Wang, Y. Y. Sun, S. Y. Dong and J. H. Sun, Solar-driven photocatalytic removal of organic pollutants over direct Z-scheme coral-branch shape Bi_2O_3/SnO_2 composites, *Mater. Charact.*, 2020, **159**, 110036.

48 K. Yu, H. B. Huang, J. T. Wang, G. F. Liu, Z. Zhong, Y. F. Li, H. L. Cao, J. Lu and R. Cao, Engineering cation defect-mediated Z-scheme photocatalysts for a highly efficient and stable photocatalytic hydrogen production, *J. Mater. Chem. A*, 2021, **9**, 7759–7766.

49 S. L. Kong, Z. H. An, W. W. Zhang, Z. H. An, M. Yuan and D. H. Chen, Preparation of hollow flower-like microspherical β-Bi_2O_3/BiOCl heterojunction and high photocatalytic property for tetracycline hydrochloride degradation, *Nanomaterials*, 2020, **10**, 57.

50 F. H. Quina and G. T. M. Silva, The photophysics of photosensitization: a brief overview, *J. Photochem. Photobiol.*, 2021, **7**, 100042.

51 M. L. Zhang, F. F. Duo, J. H. Lan, L. X. Li, J. W. Zhou, L. L. Chu and C. B. Wang, MoS_2QDs/BiOBr heterostructures for significantly enhancing visible light photocatalytic capability for the organic dyes and antibiotics removal, *Appl. Surf. Sci.*, 2022, **583**, 152544.

52 Q. H. Zhao, X. Y. Liu, Y. X. Xing, Z. L. Liu and C. F. Du, Synthesizing Bi_2O_3/BiOCl heterojunctions by partial conversion of BiOCl, *J. Mater. Sci.*, 2017, **52**, 2117–2130.